International Journal of Heat and Mass Transfer 53 (2010) 356–364

Contents lists available at ScienceDirect

International Journal of Heat and Mass Transfer

journal homepage: www.elsevier.com/locate/ijhmt

Numerical study of turbulent heat and fluid flow in a straight square duct at higher Reynolds numbers

Zuojin Zhu [1], Hongxing Yang *, Tingyao Chen

Department of Building Services Engineering, The Hong Kong Polytechnic University, Kowloon, Hung Hom, Hong Kong, PR China

A R T I C L E I N F O

Article history:
Received 1 April 2009
Received in revised form 30 August 2009
Accepted 30 August 2009
Available online 8 October 2009

Keywords:
Turbulence in a straight square duct
Heat and fluid flows
Non-standard analysis of turbulence
Passive scalar

A B S T R A C T

This paper presents the large eddy simulation (LES) results of turbulent heat and fluid flows in a straight square duct (SSD) at higher Reynolds numbers ranged from 10^4 to 10^6, which are based on the bulk mean velocity and the duct cross-sectional side length. A sub-grid model is proposed, which assumes that the sub-grid stress and heat flux are, respectively, proportional to the temporal increments of the filtered strain rate and temperature gradient, with the proportional coefficient determined by calibrating the friction factor. The temperature was taken as passive due to the neglect of buoyancy effect. The Taylor and Kolmogorov scales in the SSD are predicted and the results show that the LES results are better than c-DNS results. The LES results can explain why the c-DNS is applicable to the problem at a moderate Re, and reveal that the largest relative deviation of the overall mean Nusselt number is less than 10% as compared with existing experimental correlations. With the rise of Reynolds number, the mean secondary vortex pairs move towards the corners and have smaller size, while smaller vortices also occur in the instantaneous secondary flow. Empirical mode decomposition (EMD) was carried out to analyze the fluctuation of the *x*-averaged cross-sectional origin temperature at $\mathrm{Re} = 10^5$.

1. Introduction

The problem of turbulent heat and fluid flows in a straight square duct (SSD) is fundamental in thermal science and fluid mechanics. The turbulence in the SSD has a remarkable change in flow structure due to the existence of the so-called Prandtl's second kind secondary flows [1]. The secondary flow has a significant effect on the transport of heat and momentum as uncovered by the recent large eddy simulation (LES) [2]. Extensive studies have been pursued. Examples are the work based on the algebraic stress model of turbulence [3], those emphasizing the effect of rib roughened wall [4–7], the effect of a square bar detached from the wall [8], the effect of periodic array of cubic pin–fins in a channel [9], and the effect of inside tubes with helical fins [10].

The coarse-grid direct numerical simulation (c-DNS) [11] at a bulk mean Reynolds number of 10^4 has presented some primary characteristics of forced turbulent heat convection which is consistent with experimental observations, indicating that the c-DNS is applicable at the moderate Reynolds number and grid resolution used. However, since with the increase of Reynolds number the sub-grid eddy effect becomes more and more significant on the solution of large-scale turbulence, the c-DNS produces larger discrepancy in numerical results as compared with existing measured data.

A brief literature review is given in the previous work [11]. More developments in the study of turbulence will be introduced below. From the Navier–Stokes equations, a simple nonlinear dynamical system is developed for the delta-vee evolution , which shows the ubiquitous non-Gaussian tails in turbulence have their origin in the inherent self-amplification of the delta-vee [13]. One-dimensional Burgers turbulence driven by a white noise in time random forces has statistical properties surprisingly similar to real-life three-dimensional (3D) turbulence: Kolmogorov energy spectrum, intermittency and the scaling properties of the dissipation rate fluctuations, and bifractality of probability density function of velocity difference [14,15]. However, whether this similarity can ensure a well repetition of real-life turbulence related to fluid coherent motions [16–18] needs to be verified.

The α-NS model [19] has attracted some attention in recent years [20,21]. The non-standard analysis of turbulence [22] allows the use of c-DNS to obtain relatively accurate results at moderate Reynolds numbers [23–34]. The earlier DNS [23] indicated that turbulent statistics along the wall-bisectors agrees well with measured channel data of plane channel flow [35–38], despite the influence of the sidewalls in the former flow. For higher Reynolds number turbulence, it seems that large eddy simulation is better, and evidence can be found in previous works [39–47].

* Corresponding author. Tel.: +86 52 27665863; fax: +86 52 27746146.
E-mail addresses: behxyang@polyu.edu.hk (H. Yang), betychen@polyu.edu.hk (T. Chen).
URL: http://staff.ustc.edu.cn/~zuojin (Z. Zhu).
[1] Multiphase Reactive Flow Division, Department of Thermal Science and Energy Engineering, USTC, Hefei 230026, PR China.

0017-9310/$ - see front matter © 2009 Elsevier Ltd. All rights reserved.
doi:10.1016/j.ijheatmasstransfer.2009.09.021

Nomenclature

c_p	specific heat at constant pressure (J/kg K)	T	temperature
C_i	ith intrinsic mode function	T_τ	mean friction temperature (K)
f	mean friction factor	u, v, w	normalized velocity components
H	duct section side length (m)	U_m	balk mean velocity (m/s)
k_u	turbulence kinetic energy	u_τ	mean friction velocity (m/s)
$\overline{Nu}_{av}$	mean Nusselt number in Eq. (14)	x, y, z	Cartesian coordinates
p	normalized pressure	y^+	$= (y + 0.5)u_\tau/v$, wall coordinate
Pr	Prandtl number	Θ^+	$\equiv \theta^+/13$, normalized temperature
Q_w	heat transfer rate per unit area ($\mathrm{W/m^2}$)	ϕ	pressure potential
$\mathbf{u}$	normalized velocity vector	λ_u	Taylor scale in the unit of H
R	residue of EMD	η_u	Kolmogorov scale in the unit of H
Re	balk mean Reynolds number	v	kinematic viscosity of fluid ($\mathrm{m^2/s}$)
Re_τ	friction Reynolds number	ϵ	dissipation rate of k_u
S_{ij}	filtered strain rate	σ_θ	turbulent Prandtl number
s_{ij}	strain rate fluctuation		

This paper presents the numerical results of turbulent large-scale motion based heat and fluid flows in a SSD at various Reynolds numbers in the range from 10^4 to 10^6 at a given grid resolution with a grid number of about 1.2×10^6. The sub-grid stress and heat flux are assumed to be proportional to the temporal increments of the strain rate and temperature gradient, and the filtering is based on the so-called monad average [22]. The model coefficient is sought by calibrating the friction factor. The present sub-grid model has an advantage of elucidating why the c-DNS of turbulence at moderate Reynolds number is applicable. The temperature is taken as passive so that the buoyancy effect can be completely neglected. It is assumed that the flow Mach number is lower and the air flow can be considered as incompressible; the temperature dependence of the thermal–physical properties of air can be ignored. The temperature equation proposed in the DNS work [32] is used for the case of isoflux heating on the walls. The governing equations are solved numerically by a projection method based on a finite difference scheme [11], which is improved from the numerical work of wake flow simulation [12]. The Taylor and Kolmogorov micro-scales of turbulence in the SSD are found numerically, indicating that the grid resolution required for the traditional means DNS should be very severe.

2. Governing equations

At higher Reynolds numbers, sub-grid scale effect on large-scale motions should be carefully accounted. Additional assumptions are required in the non-standard analysis of turbulence [22]. In previous LES works [39–46], sub-grid stress is usually assumed to be the product of the eddy viscosity and the locally filtered strain rate, which is merely an analogy to the constitutive relationship in Newtonian fluid mechanics. The sub-grid model used in LES has not successfully explained at which Reynolds number the LES model should be applicable. To overcome this paradoxical problem, here we suggest an algebraic model which assumes the sub-grid stress is proportional to the temporal increment of filtered strain rate, $S_{ij} = \frac{1}{2}\left(\frac{\partial u_i}{\partial x_j} + \frac{\partial u_j}{\partial x_i}\right)$. It can be expressed by

$$-\overline{u_i' u_j'} = \frac{\alpha^2 \Delta t}{2} \frac{\partial}{\partial t}\left(\frac{\partial u_i}{\partial x_j} + \frac{\partial u_j}{\partial x_i}\right) \quad (1)$$

Here u_i' stands for the velocity fluctuation component in x_i direction, Δt denotes the time step in the simulation, and the coefficient α^2 needs to be calibrated by friction factor measured in experiments, which should be dependent on Reynolds number. Physically, α^2 stands for a kind of sub-grid viscosity. According to the results of previous studies [39,48], the sub-grid viscosity α^2 is not a constant in the presence of wall effects. Therefore, we assume that α^2 decays with the wall coordinate y^+ in a way of $[1 - \exp(-y^+/25)]^2$, where $y^+ = yu_\tau/v$, y denotes the normal distance to the wall, with u_τ denoting the mean friction velocity and v representing the kinematic viscosity of fluid.

It is noted that the sub-grid model is derived approximately from the α^2-introduced accurate projection method in the form of Eq. (8). In the approximation, the term $[\nabla \cdot (\alpha^2 \nabla \mathbf{u})]^{n+1/2}$ in the left-hand side of Eq. (8) was replaced by $[\nabla \cdot (\alpha^2 \nabla \mathbf{u})]^n$, rather than directly omitted as in the traditional methods from which the sub-grid stress should be proportional to the filtered strain rate.

Using the discretized form of temperature Eq. (11) and a similar approximation, the sub-grid heat flux can be derived to be proportional to the temporal increment of filtered temperature gradient, $\frac{\partial \Theta}{\partial x_j}$, we have

$$-\overline{u_j' \theta'} = \frac{\alpha^2 \Delta t}{2\mathrm{Pr}}\left[\frac{2\mathrm{Pr}}{\sigma_\theta}\right] \frac{\partial}{\partial t}\left(\frac{\partial \Theta}{\partial x_j}\right) \quad (2)$$

where Θ and θ' are, respectively, the monad averaged and fluctuating temperatures. The factor 1/2 is used to maintain a consistency in form with sub-grid stress model where the velocity field is divergence free for incompressible turbulence. The ratio $[\kappa = 2Pr/\sigma_\theta]$ is used to reflect the peculiarity of turbulent diffusion of temperature, where σ_θ denotes the turbulent Prandtl number. the sub-grid model based on monad filtering is expected to have the advantage of elucidating why c-DNS is possibly successful in duct flow study at a moderate Re around 10^4. Evidence will be given in this LES work.

Let the origin of the Cartesian coordinate system set at the central point of the computational domain, and the coordinates in the streamwise, transverse and spanwise directions be $x(x_1)$, $y(x_2)$ and $z(x_3)$, respectively. We further assume that the air flow in the SSD is heated under an isoflux condition, implying that the time-averaged wall heat flux does not change in the x-direction. This heating mode is equivalent to an assumption that the time-averaged wall temperature $\langle T_w \rangle$ should increase linearly in x-direction, due to the global heat balance for a fully developed thermal field. Therefore, the bulk mean temperature $\langle T_m \rangle$ should also increase linearly in the x-direction, i.e., $\partial\langle T_m\rangle/\partial x = \partial\langle T_w\rangle/\partial x = \mathrm{const}$.

Let $13T_\tau$ denote the temperature scale, the dimensionless temperature is defined as:

$$\Theta^+ = (\langle T_w \rangle - T)/(13T_\tau) \equiv \theta^+/13 \quad (3)$$

where T_τ is the friction temperature defined by $Q_w/(\rho c_p u_\tau)$. The factor 13 is used for synchronizing the computation, i.e., it allows the solution of temperature by using the same time step used in the velocity calculation. Using bulk mean velocity U_m and the duct cross-sectional side length H as the velocity and length scales in variable normalization, and inserting the sub-grid heat flux expressed by Eq. (2) into energy conservation relation, we obtain the dimensionless temperature Θ^+ equation as follows:

$$\Theta_t^+ + \mathbf{u}\cdot\nabla\Theta^+ - \frac{4u_\tau}{13U_m\int_A udA}u = \frac{1}{RePr}\nabla^2\mathbf{\Theta}^+ + \nabla\cdot\left[\frac{\kappa\alpha^2}{\mathrm{Pr}}\nabla(\mathbf{\Theta}_t^+\Delta t/2)\right] \quad (4)$$

where α^2 is normalized by HU_m, Δt is normalized by H/U_m, $dA = dydz$, is the element of cross-sectional area, u is the normalized streamwise velocity component, and u_τ is the mean friction velocity. The Reynolds number Re is defined as HU_m/ν, the Prandtl number of air $\mathrm{Pr}(=\nu/\gamma)$ is 0.71. The last term on the left-hand side of the Eq. (4) corresponds to $-u\{\partial\langle T_w\rangle^+/\partial x\}/13$, as stated by Kasagi et al. [32] in case of turbulent channel flow.

With the sub-grid stress model (1), the governing equations of the turbulent flows can be written as

$$\nabla\cdot\mathbf{u} = 0 \quad (5)$$

$$\mathbf{u}_t + \mathbf{u}\cdot\nabla\mathbf{u} = -\nabla p + \frac{1}{\mathrm{Re}}\nabla^2\mathbf{u} + \nabla\cdot[\alpha^2\nabla(\mathbf{u}_t\Delta t/2)] + \Pi\delta_{i1} \quad (6)$$

where δ_{ij} is the Kronecker delta tensor, Π represents the mean pressure gradient in the x-direction, which can be adjusted dynamically to maintain the constant mass flux in the SSD flow [49]. The initial flow field is assumed to be laminar, and perturbed by an approach incorporating the initial acceleration effect. The streamwise periodic condition is used with the non-slip conditions on the duct walls. The normalized temperature Θ^+ is zero on the SSD walls, and should be identical to $[\mathrm{Pr}\cdot u/(13u_\tau/U_m)]$ as the initial condition of the temperature field.

3. Numerical method

The temperature and velocity governing Eqs. (4)–(6) have included the sub-grid model reflecting the sub-grid eddy effect. Since the model coefficient α^2 at $y^+\to\infty$ stands for the isotropic small eddy viscosity, it is a constant dependent on the Reynolds number. By some proper changes, the existing numerical methods in DNS, such as those described in Refs. [10,50–54], are still applicable.

The solutions of the Eqs. (4)–(6) are sought by the accurate projection algorithm PmIII [55] in a non-uniform staggered grid system. Due to the further use of the sub-grid model, the solution method is given below.

Let the intermediate velocity vector, the pressure potential and the time level be denoted by $\bar{\mathbf{u}}$, ϕ and n, respectively. Assume $\mathbf{H} = (\mathbf{u}\cdot\nabla)\mathbf{u}$, then let

$$\mathbf{u}^{n+1} = \bar{\mathbf{u}} - \Delta t\nabla\phi \quad (7)$$

we can calculate $\bar{\mathbf{u}}$ by

$$\frac{\bar{\mathbf{u}}-\mathbf{u}^n}{\Delta t} + \left[\mathbf{H} + \nabla\cdot(\alpha^2\nabla\mathbf{u})\right]^{n+1/2} = \nabla\cdot\left\{\left(\frac{1}{\mathrm{Re}}+\alpha^2\right)\nabla\left[\mathbf{u}^n + \frac{1}{2}(\bar{\mathbf{u}}-\mathbf{u}^n)\right]\right\} \quad (8)$$

and calculate pressure p by

$$p^{n+1/2} = \left\{1 + \Delta t\nabla\cdot\left[\left(\frac{1}{\mathrm{Re}}+\alpha^2\right)\nabla\Big/2\right]\right\}\phi \quad (9)$$

where the pressure potential ϕ must satisfy the Poisson's equation

$$\nabla^2\phi = \nabla\cdot\bar{\mathbf{u}}/\Delta t \quad (10)$$

while the temperature Θ^{+n+1} can be calculated by

$$\frac{\Theta^{+n+1}-\Theta^{+n}}{\Delta t} + \left[H_4 + \nabla\cdot\left(\frac{\kappa\alpha^2}{\mathrm{Pr}}\nabla\Theta^+\right)\right]^{n+1/2} = \frac{1}{\mathrm{Pr}}\nabla\cdot\left\{\left(\frac{1}{\mathrm{Re}}+\kappa\alpha^2\right)\nabla\left[\Theta^{+n} + \frac{1}{2}\left(\Theta^{+n+1}-\Theta^{+n}\right)\right]\right\} \quad (11)$$

where $H_4 = [\mathbf{u}\cdot\nabla\Theta^+ - \frac{4u_\tau}{13U_m\int_A udA}u]$, and the terms at the level of $(n+1/2)$ are calculated explicitly using a second-order Euler predict-correction scheme in temporal, where spatial difference is evaluated by using the scheme similar to the previously used [11]. The pressure potential Poisson's equation is solved by the approximate factorization one (AF1) method [56]. The streamwise periodicity of pressure potential is appropriately considered in the AF1 iteration. The temperature Eq. (4) is solved by time marching. The implicit second-order Crank–Nicolson for the right-hand side diffusion terms, and fourth-order upwind scheme for the left-hand side convection terms are used in spatial discretization.

4. Results and discussion

The turbulent heat and fluid flows in a SSD at six bulk Reynolds numbers $(10^4, 5\times10^4, 10^5, 2\times10^5, 8\times10^5$, and $10^6)$ were simulated numerically, in which the turbulent Prandtl number of temperature σ_θ was set as 0.9. The simulation was conducted in the staggered grid system, where dense grids were distributed in the near wall region, with the grid distance regulated by a power law. Nearly uniform streamwise grid had the grid number of 121, that means the 15 x-directional meshes near the inlet section were amplified gradually by a factor of 1/0.9, while the 15 x-directional meshes near the exit section were shortened gradually by a factor of 0.9, the meshes in the central region were uniform. The minimum and maximum mesh lengths in the x-direction were, respectively, 0.01266 and 0.06149. Non-uniform spanwise and transverse grids had the same grid number of 101, there were 25 non-uniform meshes near each duct wall, the mesh lengths from the wall to the central region were amplified gradually by a factor of 1/0.85. Therefore, the minimum mesh length for the nearest wall mesh was 2.8×10^{-4}, while the maximum mesh length for the middle region meshes was 0.01636.

The normalized streamwise length of the computational domain was equal to 6.41, since the previous DNS study [24] has shown that the self-correlation coefficient of the streamwise velocity component is close to zero when the distance from the origin is equal to 3.2. The criterion for pressure potential iteration was chosen so that the relative error defined previously [57] should be less than 3×10^{-8}. The large eddy simulation (LES) work focuses to:

- Explore the fluid flow characteristics by calculating the turbulence statistics, the mean and secondary flows and Taylor and Kolmogorov micro-scales.
- Explore the dependence of heat and fluid flow characteristics on the Reynolds number, and reasons why the DNS and c-DNS of turbulent flows can give satisfactory results at moderate Reynolds numbers.
- Predict the Nusselt numbers of the forced turbulent heat convection in a SSD at higher Reynolds numbers, and investigate the heat transfer characteristics by illustrating the temperature fluctuation intensity and intrinsic mode functions obtained by empirical mode decomposition [58].

4.1. Turbulence statistics

Based on the average in time and streamwise direction, statistical values of turbulent variables along the wall-bisector were evaluated.The initial field was obtained by reading the unformatted temporary data file saved at the time of $t = 200$ for the Reynolds number of 10^4. To remove the effect of Reynolds number change, the numerical results in the time range from 200 to 300 were not used for the statistical analysis of turbulence. Such a time range of 100 equals 15.6 turnover times, and is sufficiently long to make the simulation results after the time of $t = 300$ become statistically steady. Hence, the time range used in the average was from $t = 300$ to 400, in which a data sequence with five thousand records was used in the analysis of turbulence statistics. The sub-grid viscosity α^2 at $y^+ \to \infty$ and mean friction factor as functions of Re were supplementarily shown in Fig. 1(a and b) and Tables 1 and 2. The sub-grid viscosity α^2 at $y^+ \to \infty$ was obtained by calibrating the friction factor with the empirical correlation of Swamee and Jain [59], which can also be found in the book of Roberson and Crowe [60].

At a higher Reynolds number, small eddies play a more important role in turbulent diffusion of mass and momentum. As shown in Table 1, the ratio of sub-grid viscosity to fluid kinematic viscosity denoted by α^2Re at $y^+ \to \infty$ becomes larger, while at a moderate Re, such as $\mathrm{Re} = 10^4$, the viscosity ratio is as small as 7.5%, elucidating why coarse-grid DNS can give satisfactory results in turbulence exploration. Using the ratio, it can also explain why the c-DNS has lost its potential in simulating the SSD flow at higher Reynolds numbers, since as soon as the mean friction factor was largely under-predicted, then significant deviations of the mean velocity profile and rms values of velocities would occur.

The mean profiles of velocity and temperature based on the sub-grid model in the LES work are compared with the analytical result from the α-NS model [19] and the existing numerical [24,40] and experimental results [36,63], as shown in Fig. 2(a and b). Along the wall-bisector, the velocity profiles at various Reynolds numbers are in good agreement with the published results, showing that the sub-grid model has an application potential. The mean temperature in almost the whole buffer layer of $y^+ \in (5, 30)$ is slightly lower when the Reynolds number increases from 10^4 to 10^5. For the case of $\mathrm{Re} = 10^6$, the nearest grid distance to the wall is around $y^+ = 10$, and the temperature profile has slightly shifted upper.

The velocity bands are defined by $[u] = \max(u) - \min(u)$, $[v] = \max(v) - \min(v)$, $[w] = \max(w) - \min(w)$, here u, v, w represent the x-averaged velocities, and the mid point of the band is adjusted so that it has the time-averaged value. The velocity bands are plotted as functions of y^+ at four Reynolds numbers, as seen in Fig. 3. The turbulent flow in the SSD at higher Reynolds numbers does have intensive velocity fluctuations, suggesting that the flow is fulfilled by the coherent structures composed of the Ω type vortices and vortical tubes and rings [17]. The outer margin is in general

Table 1
The sub-grid viscosity (α^2) and viscosity ratio at $y^+ \to \infty$ as functions of Re.

$\mathrm{Re}/10^4$	1	5	10	20	80	100
$10^5\alpha^2$	0.75	0.75	0.75	0.74	0.368	0.316
$\alpha^2\mathrm{Re}$	0.075	0.375	0.75	1.48	2.94	3.16

Table 2
The $10^2 f$ as a function Re.

$\mathrm{Re}/10^4$	1	5	10	20	80	100
$10^2 f_{\text{c-DNS}}$ [a]	3.00	1.88	1.40	1.00	0.465	0.41
$10^2 f_{\text{LES}}$ [b]	3.00	2.04	1.69	1.51	1.21	1.16
$10^2 f_{\exp}$	3.10	2.08	1.78	1.55	1.21	1.16

[a] Based on c-DNS when $\alpha^2 = 0$.
[b] Based on LES when values of α^2 in Table 1 are used.

about 2.5, except for $[v]$ at $\mathrm{Re} = 10^4$ that has larger values in the viscous sublayer ($y^+ \leqslant 5$).

A comparison of turbulence intensities is given in Fig. 4. The increase of Re leads to the outer shift of the peaks of velocity rms curves. In particular, at $\mathrm{Re} = 10^6$, the peak of u_{rms} occurs at a position of $y^+ > 100$, indicating that the grid resolution to some extend seems to be inappropriate. Evidence can also be seen in Fig. 5, where Reynolds stress comparison is shown. Merely qualitative agreement is observed for the calculated Reynolds stress at the lower three Reynolds numbers, while for $\mathrm{Re} = 10^6$, the Reynolds stress would have been largely under-predicted. The reason is that the viscosity ratio α^2Re has increased to 3.16.

4.2. Reynolds number effect

The Reynolds number effect has been partially illustrated above by turbulence statistics along the wall-bisector. To further detail the effect, the further quadrant-averaged mean and instantaneous secondary flow structures are demonstrated in Fig. 6. The mean secondary flow, as seen in Fig. 6(d–f), occurs two vortex pairs in the corner, distributing symmetrically to the duct diagonal bisector. The near wall vortices are slender than the near diagonal counter-rotating vortices, which transports the fluid between them to the duct corner. With the increase of Re, the scales of the counter-rotating vortices become smaller, and closer to the corner.

However, as seen in Fig. 6(d–f) the instantaneous secondary vortices compose of irregular and chaotic patterns. The mutually stretching of the coherent vortices [16,17] is the primary reason that generates the irregular patterns. Again, the instantaneous sec-

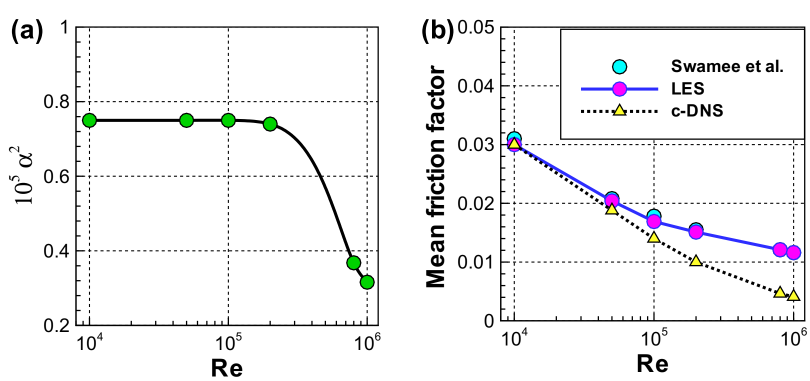

Fig. 1. The sub-grid viscosity at $y^+ \to \infty$ (a) and the friction factor (b) plotted as functions of bulk Reynolds number. Note that the value of α^2 is determined by calibrating the friction factor with the explicit expression of Swamee and Jain [59]: $f = 0.25/\{\log[k_s/(3.7H) + 5.74/\mathrm{Re}^{0.9}]\}^2$, which is introduced in the book of Roberson and Crowe [60], where the equivalent sand roughness k_s was set as zero in the calibration.

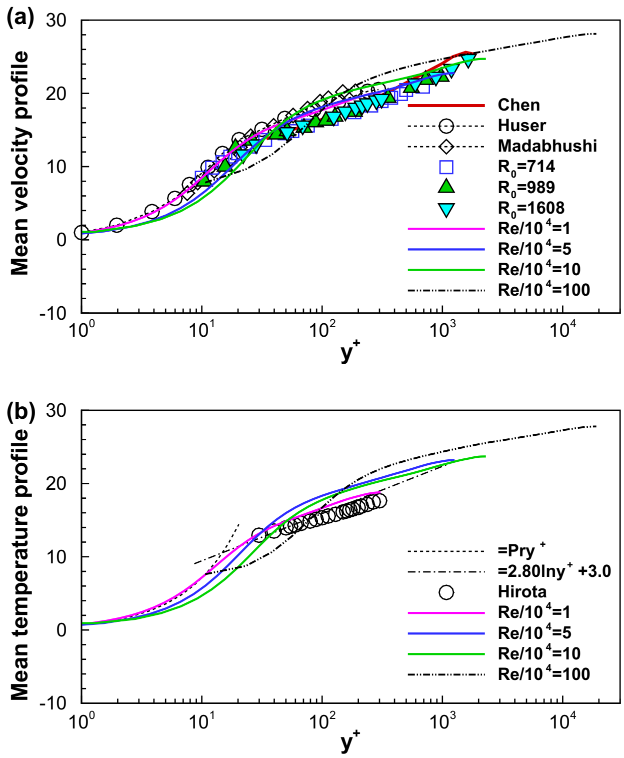

Fig. 2. The mean velocity (a) and temperature (b) profiles plotted as functions of the wall coordinate along the wall-bisector. Note that the results labeled by $R_0(=\mathrm{Re}_\tau/2)$ are based on the experiments of Wei and Willmarth [36]. R_0 denotes a friction Reynolds number based on $H/2$, its value in the work of Chen et al. [19] is around 1600. In the DNS of Huser and Biringen [24] $\mathrm{Re}_\tau = 600$, and in the LES of Madabhushi and Vanka [40] $\mathrm{Re}_\tau = 360$. While for the cases of $\mathrm{Re} = 10^4$, 5×10^4, 10^5, and 10^6 in the present study, $\mathrm{Re}_\tau = 612$, 2559, 4704, and 37910. The bulk Reynolds number in the heat transfer experiment of Hirota et al. [63] is 6.7×10^4.

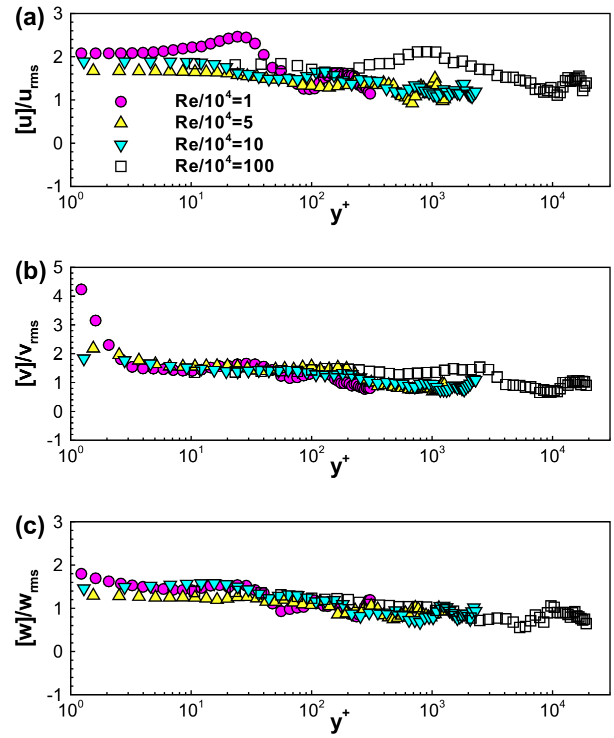

Fig. 3. The velocity variation bands along the wall-bisector plotted as functions of the wall coordinate at various Reynolds numbers. (a) $[u]/u_{\mathrm{rms}}$; (b) $[v]/v_{\mathrm{rms}}$; and (c) $[w]/w_{\mathrm{rms}}$.

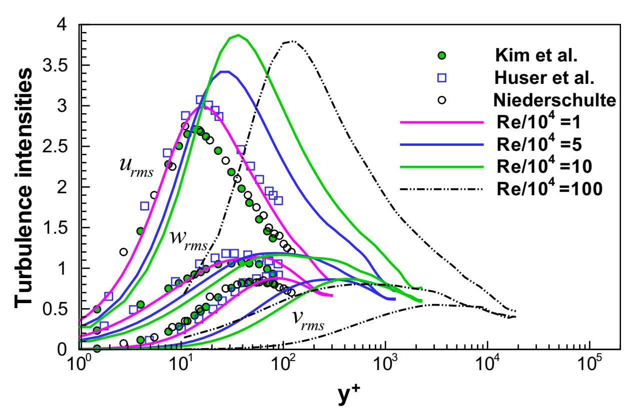

Fig. 4. The comparison of turbulence intensity along the wall-bisector with existing data. Note that the friction Reynolds number is 180 (based on the channel half-width and wall shear velocity) in the fully spectral DNS of the plane channel flow done by Kim et al. [30], and in the experiment with laser-Doppler techniques by Niederschulte et al. [37]. In the DNS of Huser and Biringen [24] $\mathrm{Re}_\tau = 600$.

ondary vortices have finer scales, with more occurring in the near wall region.

The quadrant average based distributions of the Taylor and Kolmogorov micro-scales are shown by the contours of $\log(\lambda_u)$ and $\log(\eta_u)$ at three Reynolds numbers, as seen in Fig. 7. The Taylor and Kolmogorov micro-scales λ_u are predicted by using[see in Ref. [61]]

$$\lambda_u^2 = 10\nu k_u/\epsilon, \quad \eta_u^2 \equiv (\nu^3/\epsilon)^{1/2} = \lambda_u^2\left[\nu(\epsilon/\nu)^{1/2}/(10k_u)\right] \tag{12}$$

here $k_u = \frac{1}{2}\overline{u_i'^2}$ is the time and x-averaged turbulent kinetic energy, and ϵ is the dissipation rate of k_u given by

$$\epsilon = 2\nu\overline{s_{ij}s_{ij}}, \quad s_{ij} = (\partial u_i'/\partial x_j + \partial u_j'/\partial x_i)/2 \tag{13}$$

The Taylor scale is artificially defined, and does not represent any group of eddy sizes. The Kolmogorov scale is the smallest eddy scale, but far larger than the mean free path [61]. It is seen that the Kolmogorov scale decreases with the increase of Re. It is smaller in the near wall region, and a little bit larger in the flow core. The spatial derivatives of the scale in the flow core is relatively low at a higher Reynolds number. For instance, at $\mathrm{Re} = 10^6$, $\log(\eta_u)$ in the flow core region is about -3.03 ± 0.03. The values of η_u show that the grid resolution used is largely incompatible with the turbulent flow, since the requirement for a tradition DNS of turbulent heat and fluid flows in the SSD at a Reynolds number of about 10^6 is that the grid number in y- or z-direction should be as large as 10^3. This explains why the calculated Reynolds stress peak value ($\sim$0.4) is far lower than around 0.8, which could be postulated from the measured data given at a relative low Re [Fig. 5]. The illustration of the micro-scale distribution shows that for higher Re turbulent flows LES is better, it can present quantitatively satisfied mean profiles and qualitatively consistency of the turbulence intensities, the Reynolds stress and temperature variance. However, traditional DNS needs too fine grid resolution making a personal computer incapable.

4.3. Temperature and heat transfer

The temperature in the SSD is of an increasing tendency with time in the mean temporal variation rate being larger with the rise of Re [Fig. 8]. The reason leading to this physical phenomenon is due to the isoflux heating mode. This is because the larger the Rey-

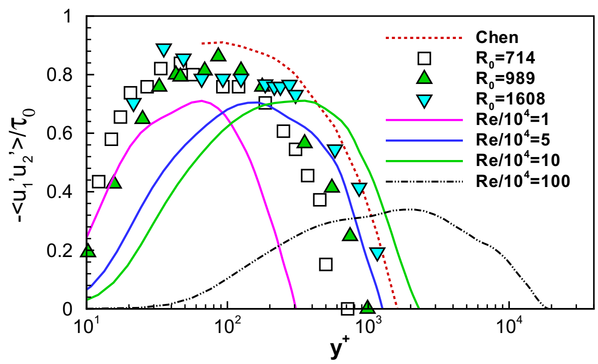

Fig. 5. The comparison of Reynolds shear stress along the wall-bisector with experiments and theoretical analysis. The R_0 in the work of Chen et al. [19] is around 1600. While the angular bracket is used to denote the time and x-averaging.

nolds number, the more important role is played by the source term $\left[\frac{4u_\tau}{13U_m\int_A udA}u\right]$ in the temperature Eq. (4).

To explore the temperature fluctuating characteristics, empirical mode decomposition (EMD) [58] is made for the historical train of the x-averaged cross-sectional origin temperature at $\mathrm{Re} = 10^5$, so that the intrinsic mode functions (IMF) can be obtained. The properties of the IMF are: (a) in the whole train, the number of extrema and the number of zero crossings must either equal or differ at most by one; (b) at any points, the mean value of the envelope defined by the local maxima and that defined by the minima should be zero. In Fig. 9, $C_i(i = 1, 2, \cdots, 7)$, is the ith IMF, the lower lever mode function has a higher frequency of intrinsic oscillation, and R is the residue of the empirical decomposition. By observing the curves of IMF in Fig. 9(a and b), it is possible to estimate approximately the intrinsic oscillating frequency of the temperature. From the monotonically temporal varying residual curve given in Fig. 9(c), it is possible to estimate the mean temporal increasing rate of the x-averaged cross-sectional origin temperature which is called as signal for EMD. In comparison with the evolution of the central point temperature at $\mathrm{Re} = 10^5$ labeled by dashed curve in Fig. 8, it is seen that the signal for EMD has lower temporal oscillating amplitudes, indicating that the x-averaging has introduced a smoothing effect.

The rms of θ^+ along the wall-bisector is shown in Fig. 10. Comparison is made between the DNS in Ref. [32], and the data in Ref. [62]. The rms curves of θ^+ is similar to the rms curves of u_{rms} given in Fig. 4, merely qualitative agreement is observed. The numerical reason is that the rms values are sensitive to the scheme of discretizing the convection terms in the governing equations, as found by Ma et al. [26].

If the time mean temperature of the air in the domain is denoted by $T_{m,av}$, then the overall mean Nusselt number of the forced heat convection in the SSD is defined by

$$\overline{Nu}_{av} = \frac{13T_\tau}{\overline{T}_w - T_{m,av}}\frac{1}{4}\int_\Gamma \frac{\partial\bar{\Theta}^+}{\partial n}d\Gamma \tag{14}$$

where Γ is the boundary of the cross-section, and $\mathbf{n}$ is the corresponding inner normal unit vector of Γ. Comparisons with the experimental correlations [64,65] can be seen in Fig. 11. The maximum relative deviation is less than 10%, suggesting that the sub-grid model is simpler and useful in accurate predicting the heat transfer rate in the particular turbulent heat and fluid flow problem.

5. Conclusions

A sub-grid model in a simpler form is developed to represent the small eddy effect on turbulent heat and fluid flows in a straight duct at higher Reynolds numbers covering the range from 10^4 to

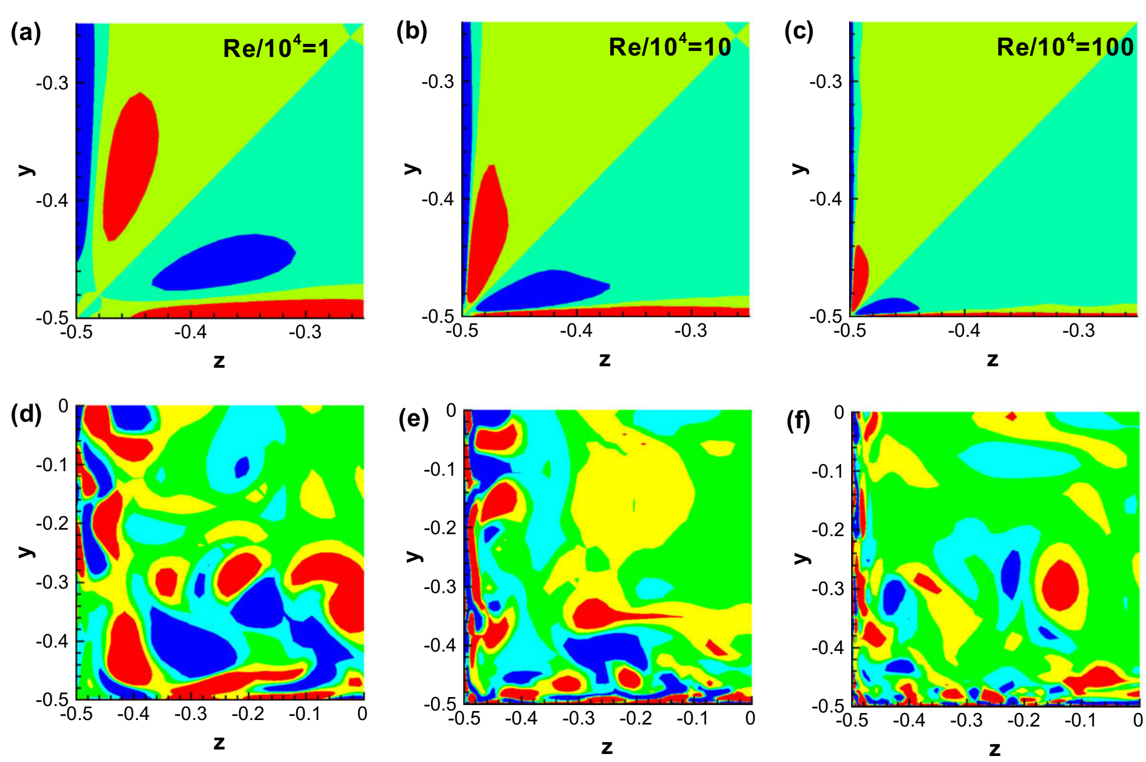

Fig. 6. The comparison of the quadrant-averaged mean secondary flows (a–c) with the instantaneous secondary flows (d–f) in the third quadrant at the time of 360 at the Reynolds number of 10^4, 10^5 and 10^6, respectively. Note that the contours in (a–c) are labeled by vorticity values of −0.5, 0, and 0.5, while the contours in (d–f) are labeled by −2, −0.5, 0.5, and 2.

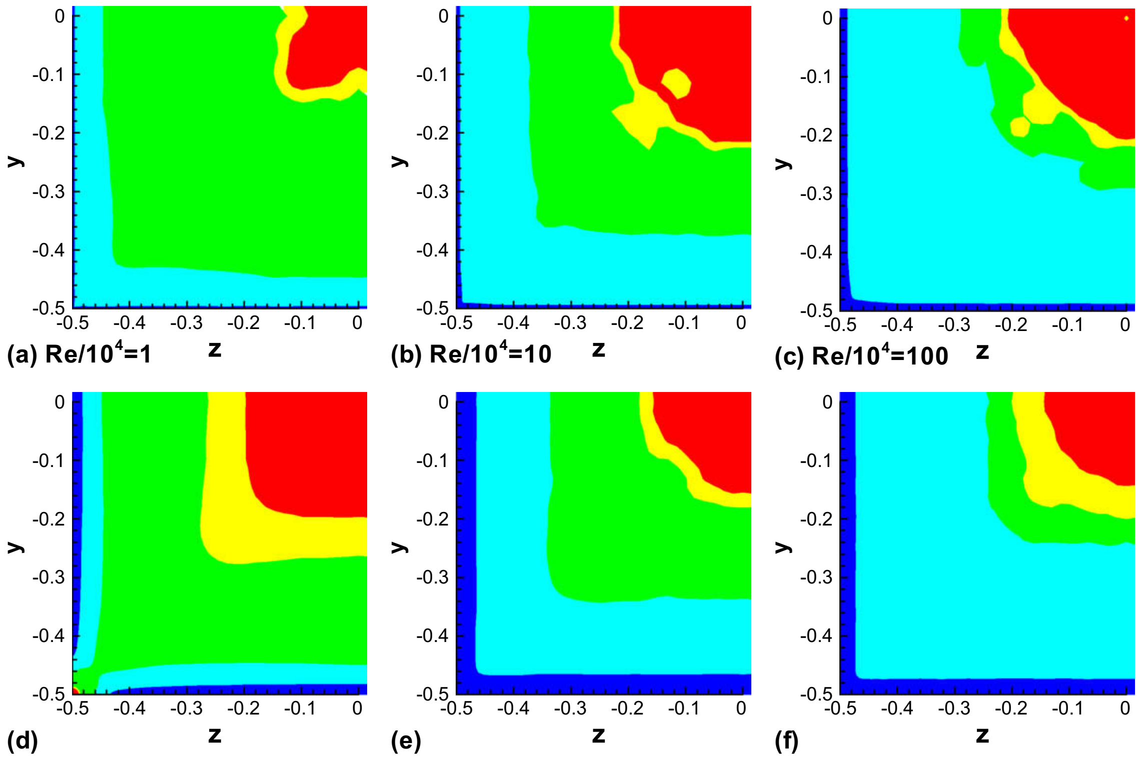

Fig. 7. The quadrant-averaged distributions of Taylor and Kolmogorov micro-scales based on estimated kinetic energy dissipation rate, where $\log(\lambda_u)$ and $\log(\eta_u)$ are shown in (a–c) and (d–f) at $\mathrm{Re} = 10^4$, 10^5, and 10^6, respectively. The $\log(\lambda_u)$ contours are labeled by −2, −1.2, −0.86, −0.85 in (a), −2, −1.2, −1.08, −1.07 in (b), −2, −1.2, −1.18, −1.17 in (c); while the $\log(\eta_u)$ contours are labeled by −2.5, −2.4, −2.15, −2.1 in (d), −3.0, −2.7, −2.59, −2.58 in (e), −3.5, −3.06. −3.03, and −3 in (f).

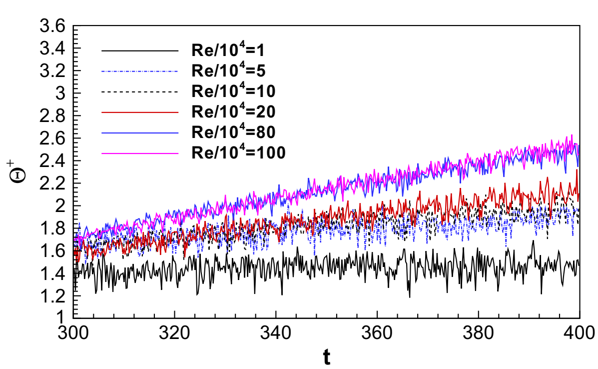

Fig. 8. The dependence of the evolution of normalized temperature at the origin point (0,0,0) on the Reynolds number, in which the data acquisition interval is set as $50\Delta t$.

10^6. By calibrating the friction factor with measured data, it is found that the sub-grid viscosity measured by the product of the bulk mean velocity and duct cross-section side length decreases monotonically from 7.5×10^{-6} to 3.16×10^{-6}, indicating at a moderate Reynolds number of 10^4 the ratio of the sub-grid viscosity to fluid kinematic viscosity is about 7.5%. This suggests the small eddy effect is negligible at moderate Reynolds numbers and the coarse-grid direct numerical simulation can give satisfactory results at the same fine grid resolution.

The quadrant-averaged mean secondary flow vortices distributed symmetrically to the duct diagonal bisectors contract to the duct corners, while the instantaneous secondary vortices fulfill the whole cross-section and have larger vorticity values as compared to that of mean secondary vortices. With the increase of Reynolds number, both kinds of vortices and the Taylor and Kolmogorov micro-scales become smaller, the deviation of the

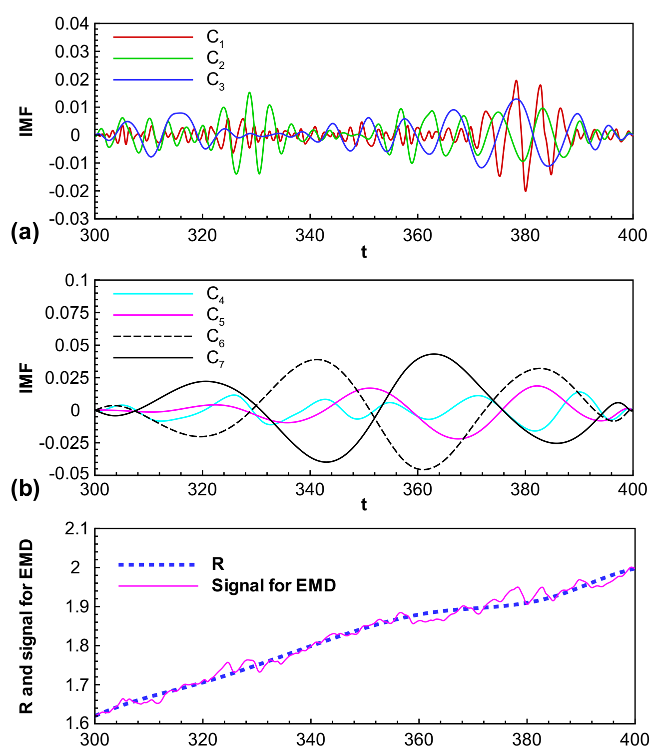

Fig. 9. The intrinsic mode functions (IMF) of x-averaged cross-sectional origin temperature in the unit of $13T_\tau$ (a and b), and the residual R and signal for the empirical mode decomposition (EMD) (c) at the Reynolds number of 10^5.

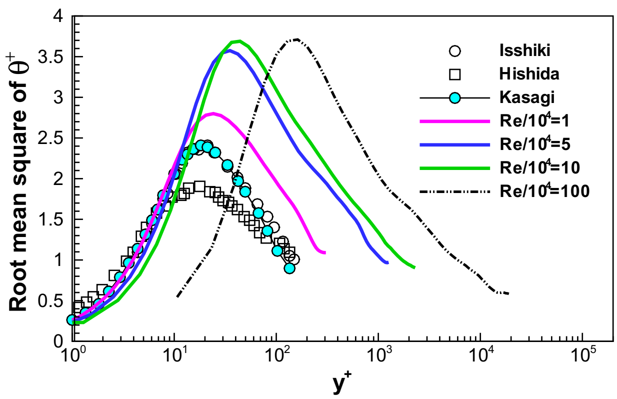

Fig. 10. The comparison of the rms curve of temperature along the wall-bisector with existing results. Note that the friction Reynolds number is 150 (based on the channel half-width and wall shear velocity) in the fully spectral DNS of the plane channel flow done by Kasagi et al. [32], and the data labeled by 'Isshiki' abstracted indirectly from [32]. The friction Reynolds number in the work of Hishida et al. [62] is 879.

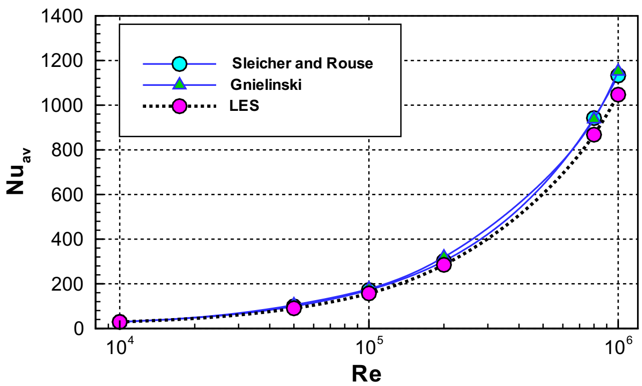

Fig. 11. The comparison of overall mean Nusselt number with experiments. Note that the correlation of Gnielinski was indirectly abstracted from Ref. [65].

overall mean Nusselt number becomes larger, and the evolution of temperature at the central point of the computational domain appears a larger temporal increasing rate, the central point temperature has a larger fluctuating amplitude in comparison with that of the *x*-averaged cross-sectional origin temperature. The evolution of the *x*-averaged cross-sectional origin temperature at the Reynolds number of 10^5 has been analyzed by the empirical mode decomposition (EMD) to explore the fluctuating characteristics. The largest relative deviation of the overall mean Nusselt number from the experimental data is found to be less than 10%. With the rise of Reynolds number, the mean secondary vortex pairs move towards the corners and have smaller size, while smaller size vortices also occur in the instantaneous secondary flow.

Acknowledgments

This work was funded by the donation from the Sun Hong Kai Properties Group. We are grateful to Prof. R.M.C. So for valuable comments, to the support of S.L. Xu, Y.Z. Liu, and NSFC (90815030).

References

[1] P. Bradshaw, Turbulent secondary flows, Annu. Rev. Fluid Mech. 19 (1987) 53–74.
[2] Z.H. Qin, R.H. Pletcher, Large eddy simulation of turbulent heat transfer in a rotating square duct, Int. J. Heat Fluid Flow 27 (2006) 371–390.
[3] G. Yang, M.A. Ebadian, Effect of Reynolds and Prandtl numbers on turbulent convective heat transfer in a three-dimensional square duct, Numer. Heat Transfer A Appl. 20 (1991) 111–122.
[4] A. Saidi, B. Sundén, Numerical simulation of turbulent convective heat transfer in square ribbed ducts, Numer. Heat Transfer A Appl. 38 (1) (2000) 67–88.
[5] K. Tatsumi, H. Iwai, K. Inaoka, K. Suzuki, Numerical analysis for heat transfer characteristics of an oblique discrete rib mounted in a square duct, Numer. Heat Transfer A Appl. 44 (8) (2003) 811–831.
[6] M. Hirota, H. Fujita, H. Yokosawa, Experimental study on convective heat transfer for turbulent flow in a square duct with robbed rough wall (characteristics of temperature field), ASME J. Heat Transfer 116 (1994) 332–340.
[7] T.T. Wong, C.W. Leung, Z.Y. Li, W.Q. Tao, Turbulent convection of air cooled rectangular duct with surface-mounted cross-ribs, Int. J. Heat Mass Transfer 46 (2003) 4629–4638.
[8] A. Valencia, Turbulent flow and heat transfer in a channel with a square bar detached from the wall, Numer. Heat Transfer A Appl. 37 (3) (2000) 289–306.
[9] A.K. Saha, S. Acharya, Unsteady simulation of turbulent flow and heat transfer in a channel with periodic array of cubic pin–fins, Numer. Heat Transfer A Appl. 46 (8) (2004) 731–763.
[10] J.H. Kim, K.E. Jansen, M.K. Jansen, Simulation of three dimensional incompressible turbulent flow inside tubes with helical fins, Numer. Heat Transfer B Fundam. 46 (3) (2004) 195–221.
[11] H.X. Yang, T.Y. Chen, Z.J. Zhu, Numerical study of forced turbulent heat convection in a straight square duct, Int. J. Heat Mass Transfer 52 (13–14) (2009) 3128–3136.
[12] J.L. Niu, Z.J. Zhu, Numerical study of three-dimensional flows around two identical square cylinders in staggered arrangements, Phys. Fluids 18 (4) (2006) 044106.
[13] Y. Li, C. Meneveau, Origin of non-Gaussian statistics in hydrodynamic turbulence, Phys. Rev. Lett. 95 (16) (2005) 164502.
[14] V. Yakhot, A. Chekhlov, Algebraic tails of probability density functions in the random-force-driven Burgers turbulence, Phys. Rev. Lett. 77 (5) (1996) 3118–3121.
[15] D. Mitra, J. Bec, R. Pandit, U. Frisch, Is multiscaling an artifact in stochastically forced Burgers equations?, Phys Rev. Lett. 94 (2005) 194501.
[16] R.J. Adrain, C.D. Meinhart, C.D. Tomkins, Vortex organization in the outer region of the boundary layer, J. Fluid Mech. 422 (2000) 1–54.
[17] V.K. Natrajan, Y. Wu, K. Christensen, Spatial signatures of retrograde spanwise vortices in wall turbulence, J. Fluid Mech. 574 (2007) 155–167.
[18] H. Wedin, D. Biau, A. Bottaro, M. Nagata, Coherent flow states in a square duct, Phys. Fluids 20 (2008) 094105.
[19] S.Y. Chen, C. Foias, D.D. Holm, E. Olson, E.S. Titi, S. Wynne, Camassa–Holm equations as a closure model for turbulent channel and pipe flow, Phys. Rev. Lett. 81 (24) (1998) 5338–5341.
[20] J.P. Graham, D.D. Holm, P.P. Mininni, A. Pouquet, Highly turbulent solutions of the Lagrangian averaged Navier–Stokes equations α model and their large-eddy simulation potential, Phys. Rev. E 76 (2007) 056310.
[21] E. Fried, M.E. Gurtin, Turbulent kinetic energy and a possible hierarchy of length scales in a generation of the Navier–Stokes α theory, Phys. Rev. E 75 (2007) 056306.
[22] F. Wu, Non-standard picture of turbulence, 2004. Available from: <http://arXiv:physics/0308012>.
[23] S. Gavrilakis, Numerical simulation of low-Reynolds-number turbulent flow through a straight square duct, J. Fluid Mech. 244 (1992) 101–129.
[24] A. Huser, S. Biringen, Direct numerical simulation of turbulent flow in a square duct, J. Fluid Mech. 257 (1993) 65–95.
[25] Y. Joung, S.U. Choi, J.I. Choi, Direct numerical simulation of turbulent flow in a square duct: analysis of secondary flows, ASCE J. Eng. Mech. 133 (2) (2007) 213–221.
[26] L.D. Ma, Z.Y. Li, W.Q. Tao, The application of high resolution finite difference scheme in direct numerical simulation of turbulent flow, J. Eng. Thermophys. 28 (5) (2007) 859–861 (in Chinese).
[27] H. Abe, H. Kawamura, Y. Matsuo, Surface heat flux fluctuations in a turbulent channel flow up to $Re_\tau = 1020$ with Pr = 0.025 and 0.71, Int. J. Heat Fluid Flow 25 (2004) 404–419.
[28] W.P. Wang, R.H. Pletcher, On the large eddy simulation of a turbulent channel flow with significant heat transfer, Phys. Fluids 8 (1996) 3354–3366.
[29] L.D. Dailey, N. Meng, R.H. Pletcher, Large eddy simulation of constant heat flux turbulent channel flow with property variations: quasi-developed model and mean flow results, ASME J. Heat Transfer 125 (2003) 27–38.
[30] J. Kim, P. Moin, R. Moser, Turbulence statistics in fully developed channel flow at low Reynolds number, J. Fluid Mech. 177 (1987) 133–166.
[31] B.Y. Li, N.S. Liu, X.Y. Lu, Direct numerical simulation of wall-normal rotating turbulent channel flow with heat transfer, Int. J. Heat Mass Transfer 49 (2006) 1162–1175.
[32] N. Kasagi, Y. Tomita, A. Kuroda, Direct numerical simulation of passive scalar field in a turbulent channel flow, ASME J. Heat Transfer 114 (1992) 598–606.
[33] N. Kasagi, N. Shikazono, Contribution of direct numerical simulation to understanding and modelling turbulent transport, Proc. R. Soc. Lond. A 45 (1995) 257–292.
[34] N. Kasagi, N. Shikazono, Direct numerical simulation of combined forced and natural turbulent convection in a vertical plane channel, Int. J. Heat Fluid Flow 18 (1997) 88–99.
[35] H.P. Kreplin, H. Eckelmann, Behavior of the three fluctuating velocity components in the wall region of a turbulent channel flow, Phys. Fluids 22 (1979) 1233–1239.

[36] T. Wei, W.W. Willmarth, Reynolds number effects on the structures of a turbulent channel flow, J. Fluid Mech. 204 (1989) 57–95.
[37] M.A. Niederschulte, R.J. Adrian, T.J. Hanratty, Measurement of turbulent flow in a channel at low Reynolds numbers, Exp. Fluids 9 (1990) 222–230.
[38] I.N. Wardana, T. Ueda, M. Mizomoto, Effect of strong heating on turbulence statistics of a channel flow, Exp. Fluids 18 (1994) 87–94.
[39] P. Moin, J. Kim, Numerical investigation of turbulent channel flow, J. Fluid Mech. 118 (1982) 341–377.
[40] R.K. Madabhushi, S.P. Vanka, Large eddy simulation of turbulence-driven secondary flow in a square duct, Phys. Fluids A 3 (11) (1991) 2734–2745.
[41] M.D. Su, R. Friedrich, Investigation of fully developed turbulent flow in a straight duct with large eddy simulation, ASME J. Fluid Eng. 116 (4) (1994) 677–684.
[42] M.S. Vázquez, O. Métais, Large-eddy simulation of the turbulent flow through a heated square duct, J. Fluid Mech. 453 (2002) 201–238.
[43] O. Métais, M. Lesieur, New trend in large eddy simulation of turbulence, Annu. Rev. Fluid Mech. 28 (1996) 45–82.
[44] E. Lamballais, M. Lesieur, O. Métais, Probability distribution function and coherent structures in a turbulent channel, Phys. Rev. E 56 (1997) 6761–6766.
[45] J. Pallares, L. Davidson, Large-eddy simulations of turbulent flow in a rotating square duct, Phys. Fluids 12 (2000) 2878–2894.
[46] J. Pallares, L. Davidson, Large-eddy simulations of turbulent heat transfer in stationary and rotating square ducts, Phys. Fluids 14 (2002) 2804–2816.
[47] D. Home, M.F. Lightstone, M.S. Hamed, Validation of DES-SST based turbulence model for a fully developed turbulent channel flow problem, Numer. Heat Transfer A Appl. 55 (4) (2009) 337–361.
[48] R.M.C. So, Y.G. Lai, H.S. Zhang, B.C. Hwang, Second-order near-wall turbulence closures: a review, AIAA J. 29 (11) (1991) 1819–1835.
[49] R.D. Moser, J. Kim, N.N. Mansour, Direct numerical simulation of turbulent channel flow up to $Re_\tau = 590$, Phys. Fluids 11 (4) (1999) 943–945.
[50] P. Le Quéré, T.A.D. Roquefort, Computation of natural convection in two-dimensional cavities with Chebyshev polynomials, J. Comput. Phys. 57 (1985) 210–228.
[51] N. Nikitin, Finite-difference method for incompressible Navier–Stokes equations in arbitrary orthogonal curvilinear coordinates, J. Comput. Phys. 217 (2006) 759–781.
[52] S.V. Patankar, Numerical Heat Transfer and Fluid Flow, Hemisphere, New York, 1980.
[53] E. Papanicolaou, Y. Jaluria, Transition to a periodic regime in mixed convection in a square cavity, J. Fluid Mech. 239 (1992) 489–509.
[54] K. Khanafer, K. Vafai, M. Lightstone, Mixed convection heat transfer in two dimensional open-ended enclosures, Int. J. Heat Mass Transfer 45 (26) (2002) 5171–5190.
[55] D.L. Brown, R. Cortez, M.L. Minion, Accurate projection methods for the incompressible Navier–Stokes equations, J. Comput. Phys. 168 (2001) 464–499.
[56] T.J. Baker, Potential flow calculation by approximation factorization method, J. Comput. Phys. 42 (1981) 1–19.
[57] Z.J. Zhu, H.X. Yang, Numerical investigation of transient laminar natural convection of air in a tall cavity, Heat Mass Transfer 39 (2003) 579–587.
[58] N.E. Huang, Z. Shen, S.R. Long, A new view of nonlinear water waves: the Hilbert spectrum, Annu. Rev. Fluid Mech. 31 (1999) 417–457.
[59] P.K. Swamme, A.K. Jain, Explicit equations for pipe flow problems, J. Hydraul. Div. ASCE 102 (1976) Hy5.
[60] J.A. Roberson, C.T. Crowe, Engineering Fluid Mechanics, John Wiley & Sons, New York, 1997.
[61] H. Tennekes, J.L. Lumley, A First Course in Turbulence, MIT Press, Cambridge, 1974. pp. 146–195.
[62] M. Hishida, Y. Nagano, M. Tagawa, Transport process of heat and momentum in the wall region of turbulent pipe flow, in: C.L. Tian (Ed.), Proceedings of the Eighth International Heat Mass Transfer Conference, Hemisphere, Washington, vol. 3, 1986, pp. 925–930.
[63] M. Hirota, H. Fujita, H. Yokosawa, H. Nakai, H. Itoh, Turbulent heat transfer in a square duct, Int. J. Heat Fluid Flow 18 (1997) 170–180.
[64] C.A. Sleicher, M.W. Rouse, A convenient correlation for heat transfer to constant and variable properties fluids in turbulent pipe flow, Int. J. Heat Mass Transfer 18 (1975) 677–683.
[65] W. Kays, M. Crawford, B. Weigand, Convective Heat and Mass Transfer, fourth ed., McGraw-Hill, New York, 2005. pp. 299.